

Accurate Gaussian Process Distance Fields with applications to Echolocation and Mapping

Cedric Le Gentil*, Othmane-Latif Ouabi^{†‡}, Lan Wu*, Cedric Pradalier[‡] and Teresa Vidal-Calleja*

*Robotics Institute, University of Technology Sydney, Australia

Email: {cedric.legentil; lan.wu-2; teresa.vidalcalleja }@uts.edu.au

[†]Sysnav, France

Email: othmane.ouabi@sysnav.fr

[‡]International Research Lab 2958 Georgia Tech-CNRS, France

Email: cedricp@georgiatech-metz.fr

Abstract—This paper introduces a novel method to estimate distance fields from noisy point clouds using Gaussian Process (GP) regression. Distance fields, or distance functions, gained popularity for applications like point cloud registration, odometry, SLAM, path planning, shape reconstruction, etc. A distance field provides a continuous representation of the scene. It is defined as the shortest distance from any query point and the closest surface. The key concept of the proposed method is a *reverting* function used to turn a GP-inferred occupancy field into an accurate distance field. The reverting function is specific to the chosen GP kernel. This paper provides the theoretical derivation of the proposed method and its relationship to existing techniques. The improved accuracy compared with existing distance fields is demonstrated with extensive simulated experiments. The level of accuracy of the proposed approach allows for novel applications that rely on precise distance estimation. Thus, alongside 3D point cloud registration, this work presents echolocation and mapping frameworks using ultrasonic guided waves sensing metallic structures. These methods leverage the proposed distance field in physics-based models to simulate the signal propagation and compare it with the actual signal received. Both simulated and real-world experiments are conducted to demonstrate the soundness of these frameworks.

Index Terms—Distance field, ultrasound, localisation, mapping.

I. INTRODUCTION

Robotics perception is a key component of any successful robotic system operating in the real world. The ability to sense and interpret the surrounding environment is crucial for navigation, planning, and overall systems performance. The choice of map representation to model the environment plays a vital role in the perception process. There are a plethora of map representations in the literature, each with its own specific set of applications. For example, dense 3D geometric point clouds are often used for lidar Simultaneous Localisation And Mapping (SLAM), while abstract sparse semantic maps are great tools for high-level decision-making. This paper introduces a novel continuous distance field representation based on Gaussian Process (GP) regression with a wide variety of applications such as localisation, mapping, and planning.

A distance field is a continuous function over a given space \mathbb{R}^N that maps a query point \mathbf{x} with the distance d to the nearest object. In this paper, we will use the term *surface* to denote the outer layer of all the objects in the scene. For some

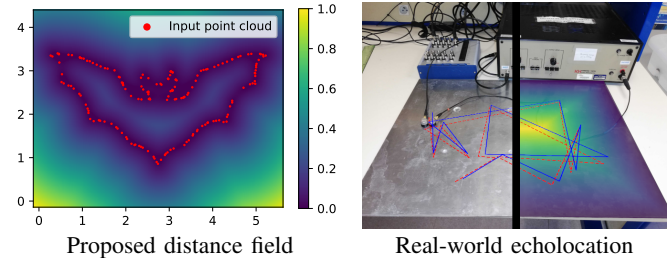


Fig. 1. Illustration of the proposed GP-based distance field. Given a point cloud, the proposed method successfully interpolates between the data points and provides an accurate distance field (left). This can be used in a wide range of applications (odometry, mapping, planning, etc). One of them is the problem of echolocation on metallic structures. The right image shows our real-world experimental setup with an ultrasonic emitter-receiver (ground truth trajectory in blue, estimated trajectory in dashed red, and overlay of the GP-based distance field on the right half).

regular-shaped objects, the surface can be represented with a *parametric* or *implicit* function that equals zero on the surface. The knowledge of such a function (e.g., $ax + by + cz + w = 0$ for an infinite plane) may lead to a closed-form expression of the distance field. In the general case, the surface function and the distance field are not explicitly known and in the context of robotics perception, surfaces are often represented with discrete samples in the form of noisy point clouds. Inspired by Gaussian Process Implicit Surface (GPIS) [1] and LogGPIS [2, 3], the proposed method leverages kernel-based GP regression [4] as a framework for interpolation between the surface samples and generates an *occupancy field* over the space. This occupancy field is then transformed into a distance field by applying a *reverting* function deduced from the GP covariance kernel. As illustrated in Fig. 1, this approach alleviates drawbacks from LogGPIS (non-Euclidean field and limited interpolation abilities [5]), thus offering both more flexibility and better accuracy.

As per its similarity with LogGPIS [3], the proposed representation enables point cloud registration (odometry, SLAM, etc) and planning. Furthermore, our method allows for new distance field applications thanks to its improved accuracy. In this paper, we demonstrate the use of Ultrasonic Guided Waves (UGWs) with co-located, omnidirectional emitter-receivers on

metallic plates for robotic navigation and inspection. The availability to query accurate distances with the nearest surface allows for the use of physics-based models of wave propagation in the measurement model of the proposed echolocation and mapping frameworks. Similarly to [6, 7] we rely on the comparison between the actual echoes of the excitation signal and simulated received measurements.

In summary, the contributions outlined in this work are the derivation of a novel GP-based distance field using point clouds as input, the thorough evaluation of the proposed distance field, and its integration into echolocation and mapping frameworks using UGWs. We also provide examples of 3D point cloud registration for comparison with applications in [3].

II. RELATED WORK

When designing a robotics perception system, the choice of map representation is primarily dictated by its use, but also by the computational power and memory available. During the early stages of robotic state estimation, most systems relied on sparse geometric feature maps for localisation [8]. These were lightweight and allowed for real-time operation with limited onboard computational power. However, this type of representation cannot really be used for any other purpose and is tied to the modality that it has been created with: a sonar feature map cannot be reused within a visual-based system. Additionally, the sparsity of such maps does not allow for safe exploration or path planning. While feature maps are still part of many recent odometry and SLAM algorithms [9, 10, 11], we see more and more alternative representations that present denser information. Using the original concept of occupancy grid [12] to represent the environment with discrete cells, frameworks like [13, 14] allow for dense mapping and path planning. Occupancy grids are a great tool for planning and exploration as each cell contains traversability information of the space (free/occupied/unknown) [15]. Other works extended the concept of occupancy grid to continuous and probabilistic representations [16, 17].

For the sake of dense 3D reconstruction, KinectFusion [18] uses the widespread Truncated Signed Distance Function (TSDF) [19] to represent the scene observed with an RGB-D camera. The truncated nature of such distance field is not necessarily compatible with planning frameworks like [20] and [21]. The use of Euclidean Signed Distance Field (ESDF) [22] in recent works like [23, 24, 25] shows the current interest of the mapping and planning community in accurate distance fields. This interest allied with the current computational power of GPUs led to the development of neural-network-based continuous representations for 3D modelling and mapping [26, 27, 28, 29]. Several works build upon such representations for the purpose of SLAM [30, 31, 32] and path planning [33, 34, 35].

Closer to the proposed method, the GPIS [1] is a probabilistic framework for surface reconstruction based on noisy observations. The work in [36] extends the GPIS to provide a signed distance function in the vicinity of the surface.

More recently, LogGPIS [2] expands the distance field to the full space. Inspired by the heat kernel methods for geodesic distance computation in the field of differential geometry [37], LogGPIS is derived using Varadhan’s results [38] to approximate the distance field by simulating heat propagation in the space. While LogGPIS demonstrates abilities for localisation and mapping (through point cloud registration), and path planning [3], the LogGPIS distance field suffers a trade-off between its ability to interpolate between the input data and the accuracy of the field away from the surface ([5]). Accordingly, LogGPIS cannot be used for applications such as echolocation where highly accurate distance fields are required regardless of the distance to the surface.

Localisation and mapping based on range measurements is an active field of study. It finds a wide range of applications such as acoustic room geometry reconstruction [39, 40], underwater localisation and mapping [41, 42], and robotic inspection [43, 44]. Yet, recent works often rely on strong assumptions on the map. For example, the latter is assumed to consist of a set of line reflectors in [39, 40, 44], preventing the possibility to capture richer information on the environment. The accuracy of the proposed GP-based distance field allows us to explore such applications in particular the problems of echolocation and mapping with UGWs.

III. METHOD

This section presents the proposed distance field theory. As it heavily relies on GPs, we first provide the reader with a brief introduction to GP regression, a probabilistic non-parametric method for interpolation.

A. Preliminaries

Let us consider an unknown signal $h(\mathbf{x}) \in \mathbb{R}$ with $\mathbf{x} \in \mathbb{R}^m$, and Q noisy observations y_i defined as

$$y_i = h(\mathbf{x}_i) + \eta_i, \quad \text{where } \eta_i \sim \mathcal{N}(0, \sigma^2). \quad (1)$$

where $i = (1, \dots, Q)$. The goal is to infer the distribution (mean and variance) of h for any given input \mathbf{x} .

By modelling the signal h as a GP $h \sim \mathcal{GP}(0, k_h(\mathbf{x}, \mathbf{x}'))$, with k_h the covariance kernel function $k_h(\mathbf{x}, \mathbf{x}') = \text{cov}(h(\mathbf{x}), h(\mathbf{x}'))$, one can express occurrences of h as a multivariate Gaussian distribution

$$\begin{bmatrix} \mathbf{y} \\ h(\mathbf{x}^*) \end{bmatrix} = \mathcal{N}\left(0, \begin{bmatrix} \mathbf{K}_h(\mathbf{X}, \mathbf{X}) + \sigma_h^2 \mathbf{I} & \mathbf{k}_h(\mathbf{x}^*, \mathbf{X})^\top \\ \mathbf{k}_h(\mathbf{x}^*, \mathbf{X}) & k_h(\mathbf{x}^*, \mathbf{x}^*) \end{bmatrix}\right), \quad (2)$$

where $\mathbf{y} = [y_1, \dots, y_Q]^\top$, \mathbf{x}^* is a query point, $\mathbf{k}_h(\mathbf{x}^*, \mathbf{X}) = [k_h(\mathbf{x}^*, \mathbf{x}_1), \dots, k_h(\mathbf{x}^*, \mathbf{x}_Q)]$, and $\mathbf{K}_h(\mathbf{X}, \mathbf{X}) = [k_h(\mathbf{x}_1, \mathbf{x}_1), \dots, k_h(\mathbf{x}_1, \mathbf{x}_Q)]$. By conditioning (2) with respect to the noisy observations, the mean and variance of $h(\mathbf{x}^*)$ are respectively computed as

$$\begin{aligned} \hat{h}(\mathbf{x}^*) &= \mathbf{k}_h(\mathbf{x}^*, \mathbf{X}) (\mathbf{K}_h(\mathbf{X}, \mathbf{X}) + \sigma_h^2 \mathbf{I})^{-1} \mathbf{y}, \quad \text{and} \\ \text{var}(h(\mathbf{x}^*)) &= k_h(\mathbf{x}^*, \mathbf{x}^*) - \\ &\quad \mathbf{k}_h(\mathbf{x}^*, \mathbf{X}) (\mathbf{K}_h(\mathbf{X}, \mathbf{X}) + \sigma_h^2 \mathbf{I})^{-1} \mathbf{k}_h(\mathbf{x}^*, \mathbf{X})^\top. \end{aligned} \quad (3)$$

B. Gaussian Process distance fields

Considering a surface \mathcal{S} in Euclidean space \mathbb{R}^m , let us define the distance field $d(\mathbf{x})$ with $\mathbf{x} \in \mathbb{R}^m$ as a scalar-valued continuous function that represents the shortest distance between the input \mathbf{x} and the surface \mathcal{S} . Such a function is a solution to the Eikonal equation

$$|\nabla d(\mathbf{x})|=1 \quad \text{with} \quad d(\mathbf{x})=0 \iff \mathbf{x} \in \mathcal{S}. \quad (4)$$

Given a set of points on the surface, the aim is to estimate the Euclidean distance \hat{d} . Unfortunately, as per its non-linear nature, the Eikonal equation (4) does not possess a known general closed-form solution. In this work, we approach the distance field estimation under the scope of *occupancy field* and GP regression. We later relate our approach to heat-based distance methods like [37] and [2].

Let us consider a set of points \mathbf{x}_i on the surface \mathcal{S} and a continuous scalar-valued field over \mathbb{R}^3 that we refer to as the occupancy field $o(\mathbf{x})$. Arbitrarily, we set the observed value of the occupancy field to one at the locations $\mathbf{x}_i \in \mathcal{S}$. Note that this approach differs from the definitions of GPIS where the field is positive inside the object, negative outside, and the surface corresponds to the zero crossing of the field. By modelling the occupancy field with a GP

$$o(\mathbf{x}) \sim \mathcal{GP}(0, k_o(\mathbf{x}, \mathbf{x}')), \quad (5)$$

we can infer the occupancy at any point $\mathbf{x} \in \mathbb{R}^m$ using (3):

$$\hat{o}(\mathbf{x}) = \mathbf{k}_o(\mathbf{x}, \mathbf{X}) (\mathbf{K}_o(\mathbf{X}, \mathbf{X}) + \sigma_o^2 \mathbf{I})^{-1} \mathbf{1}. \quad (6)$$

By considering a monotonic, stationary, isotropic kernel with an infinite domain (i.e., a non-zero, distance-based kernel), let us define a *reverting* function r as

$$r(k_o(\mathbf{x}, \mathbf{x}')) = \|\mathbf{x} - \mathbf{x}'\|, \quad (7)$$

thus the proposed distance field is

$$\hat{d}(\mathbf{x}) = r(\hat{o}(\mathbf{x})). \quad (8)$$

Please note that the occupancy field is not explicitly upper-bounded meaning that the inferred occupancy values above one are possible. As this scenario can only occur between noisy measurements of a single surface, we can safely define the distance to be zero where the occupancy value is above one.

1) *Intuitive interpretation:* To provide the reader with an intuition about the proposed method, let us first consider a 1D scenario with only one noiseless data point on the surface. The inference of the occupancy field provided by (7) is then reduced to $\hat{o}(x) = k_o(x, x_1)$. In that scenario, the reverting kernel function provides the exact distance between the surface and the query point x . As illustrated in Fig. 2 (left and middle), if we consider a set of noisy points close to the surface instead of a single noiseless measurement, the shape of the occupancy field is similar to the ideal 1D noise-free case. Without loss of generality, our method extends this reasoning to higher dimensions assuming that the occupancy field along the normal vectors to the surface is equivalent to the 1D scenario (c.f. Fig. 2 right).

	Covariance kernel ($k_o(d)$)	Reverting function ($r(o)$)
Rational quadratic	$\sigma^2 \left(1 + \frac{d^2}{2\alpha l^2}\right)^{-\alpha}$	$\sqrt{2\alpha l^2} \left(\left(\frac{o}{\sigma^2}\right)^{-\frac{1}{\alpha}} - 1 \right)$
Square exp.	$\sigma^2 \exp\left(-\frac{d^2}{2l^2}\right)$	$\sqrt{-2l^2 \log\left(\frac{o}{\sigma^2}\right)}$
Matérn $\nu = 1/2$	$\sigma^2 \exp\left(-\frac{d}{l}\right)$	$-l \log\left(\frac{o}{\sigma^2}\right)$
Matérn $\nu = 1$	$\sigma^2 \frac{\sqrt{2d}}{l} B\left(-\frac{\sqrt{2d}}{l}\right)$	$\operatorname{argmin}_d \ o - k_o(d)\ ^2$
Matérn $\nu = 3/2$	$\sigma^2 \left(1 + \frac{\sqrt{3d}}{l}\right) \exp\left(-\frac{\sqrt{3d}}{l}\right)$	$\operatorname{argmin}_d \ o - k_o(d)\ ^2$

TABLE I
COVARIANCE KERNELS AND ASSOCIATED REVERTING FUNCTIONS (B IS THE MODIFIED BESSEL FUNCTION OF THE SECOND KIND).

2) *Kernels and reverting functions:* As aforementioned, the proposed method relies on the pair kernel/reverting function to accurately estimate the distance field. This subsection discusses the case of the Rational Quadratic (RQ) kernel, the Square Exponential (SE) kernel, and a few other kernels from the Matérn family. These kernels, in their isometric form, depend on the Euclidean distance between the two input vectors. Accordingly, via a simple change of variables, they can be expressed as a function of a non-negative scalar value $d = \|\mathbf{x} - \mathbf{x}'\|$. Table I shows the different kernels considered in this work as well as their reverting function (with σ^2 as the scaling factor, and l the kernel’s lengthscale). In the case of the RQ, SE, and $\nu = 1$ Matérn kernels, it is straightforward to find the reverting function with simple algebraic manipulations. Unfortunately, for the other values of ν , the Matérn kernel does not possess a known, closed-form reverting function. In these scenarios, the reverting “function” can be formulated as a single-value non-linear optimisation problem.

3) *Kernel hyper-parameters:* As exposed in Table I, all the kernels we consider in this work depend on a scaling factor σ^2 and a lengthscale l . While we arbitrarily fix $\sigma = 1$, the value of the lengthscale depends on the data at hand as it corresponds to the typical distance at which the data points are correlated. Intuitively, l represents the “level of interpolation” as it characterises the “area of influence” of each of the observed points on the surface. In Fig. 3, we show the effect of varying the lengthscale for two non-collocated surface points. The dashed lines correspond to the ideal occupancy values that lead to true distance through the reverting function for both the hypotheses of one surface in the middle (green) and two distinct surfaces (blue). One can see that with a large lengthscale l , the occupancy field interpolates between the data points. In that configuration, the data are interpreted as noisy measurements of a single surface located in the middle. With a small l value, the observations are decorrelated allowing for the distance to be calculated in that interval. In such a case, the data are interpreted as two distinct surfaces.

As a rule of thumb, the precision of the distance field in “corridor-like” scenarios improves when decreasing l (reducing the perturbation between distinct surfaces), however, the method can lose its interpolation abilities. On the other hand, a large lengthscale reduces the level of details that can be

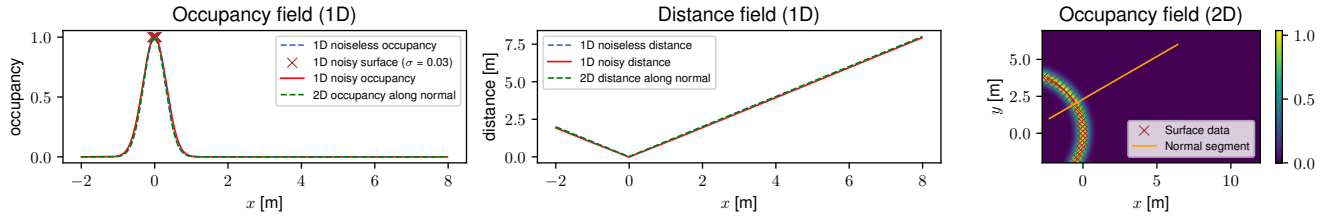


Fig. 2. Occupancy fields (1D and 2D) and corresponding distance according to the *reverting* function. The “2D” plots in the left and middle correspond, respectively, to the occupancy and distance along the normal segment (in orange) in right. This figure is obtained using the square exponential kernel.

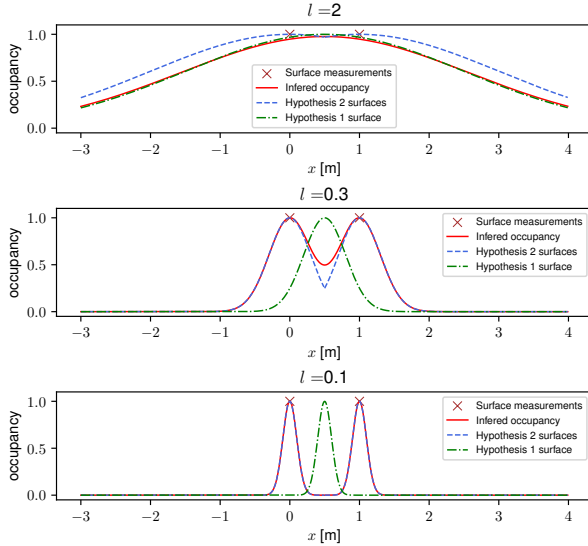


Fig. 3. Influence of the kernel’s lengthscale l on the occupancy field (1D example). Given two surface measurements (crosses), a large l (top) interprets the data as noisy measurements of a single surface in the middle. A small l (bottom) corresponds to the hypothesis of two distinct surfaces. This figure is obtained using the square exponential kernel.

captured in the distance field. It is important to note that due to the occupancy field being close to zero far from the surface, numerical accuracy issues can occur (accentuated by small values of l). We empirically noticed that the square exponential kernel is more prone to numerical issues. In summary, while it is safe to define l empirically equal to one and a half times the typical distance between neighbour data points, the choice of l is data dependent and will deserve more attention in future work (e.g., hyperparameter learning [4]).

C. Link with heat-based method

In [37], Crane *et al.* derived an optimisation-based method for accurate geodesic distance estimation built upon the heat equation ($\dot{u}_t = \Delta u_x$). Later, [2, 3] introduced the LogGPIS leveraging both GPs and concepts from [37] to perform distance field estimation in \mathbb{R}^m . The key idea in [3] is the physics-based GP approximation of the heat dispersion from the surface after a small quantum of time. Based on Varadhan’s results [38], the LogGPIS essentially corresponds to the inference of the occupancy field as presented in this work with a $\nu = 3/2$ Matérn kernel using a small lengthscale l , and a scaled negative logarithm as the reverting function to obtain

the distance. This corresponds to a close-range approximation of our proposed method. Considering small distances d , one can approximate the kernel as

$$\lim_{d \rightarrow 0} \left(1 + \frac{\sqrt{3}d}{l} \right) \exp \left(-\frac{\sqrt{3}d}{l} \right) \approx \exp \left(-\frac{\sqrt{3}d}{l} \right). \quad (9)$$

Accordingly, this approximation possesses the following reverting function: $\tilde{r}(o) = -\frac{l}{\sqrt{3}} \log(o)$. This derivation explains the “empirical” scaling value mentioned in [2].

These results corroborate statements from [5]: LogGPIS distance field is valid close to the surface but does not correspond to accurate Euclidean distances further from it. Additionally, unlike the proposed method, the accuracy of LogGPIS is negatively impacted by using larger lengthscales, leading to a trade-off between accuracy and the ability to interpolate between data points [5] (a small lengthscale can lead to the decorrelation of the data points). These observations will be verified in the experimental section of the present paper.

D. Other considerations

1) *Variance*: As shown in (3), GP regression does not only provide the inferred mean but also its variance. Similarly to [3], by propagating the occupancy uncertainty through the reverting function by using its derivative $\partial r(o)/\partial o$, the variance of the inferred distance is

$$\text{var} \left(\hat{d}(\mathbf{x}) \right) = \frac{\partial r(o)}{\partial o} \text{var} (o(\mathbf{x})) \frac{\partial r(o)}{\partial o}. \quad (10)$$

Unfortunately, we believe this variance measure does not accurately model the actual behaviour of the inferred distance field. Let us consider the $\nu = 1/2$ Matérn kernel and its reverting function. The derivative $\partial r(o)/\partial o = -l/o$ ($\sigma = 1$). Accordingly, for query points further and further away from the surface, the occupancy will decrease toward zero, leading $\text{var} \left(\hat{d}(\mathbf{x}) \right)$ to tend toward infinity. This does not correspond to the actual behaviour of the distance field (cf. empirical observations in the experiment section). Addressing this issue and proposing an appropriate uncertainty model are part of our future work.

2) *Field gradient*: In robotics applications, the distance field is often used as part of a cost function for optimisation-based state estimation. Such applications require the field’s gradient to allow for the computation of the cost function’s Jacobian. Via the application of linear operators to GPs [45],

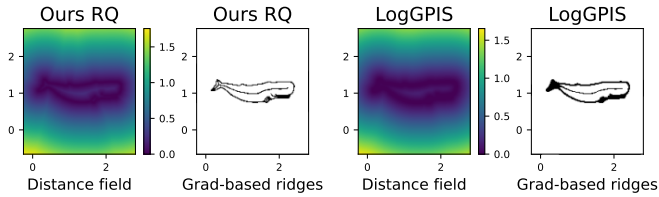


Fig. 4. Qualitative comparison of the proposed distance field and LogGPIS and their respective “ridges” (extracted with a threshold on the norm of the field’s gradient).

one can obtain the occupancy field’s gradient as

$$\nabla o = \nabla \mathbf{k}_o(\mathbf{x}, \mathbf{X}) (\mathbf{K}_o(\mathbf{X}, \mathbf{X}) + \sigma_h^2 \mathbf{I})^{-1} \mathbf{1}. \quad (11)$$

The gradient of the distance field is computed using the chain rules with ∇o and the derivative of the reverting function with respect to the occupancy $\partial r(o)/\partial o$. In the case of the optimisation-based reverting functions, we use the inverse function rule to compute $\partial r(o)/\partial o$ from $\partial k_o(d)/\partial d$. Please note that $\nu = 1/2$ Matérn kernel function is C^0 as not differentiable in at zero. Therefore the aforementioned method is not applicable in all scenarios for that particular kernel.

IV. APPLICATIONS

As both LogGPIS [3] and the proposed method are using a monotonic function over a GP occupancy field, the resultant distance fields share some properties. As shown in Fig. 4, both methods’ distance fields have “ridges” in the same areas (i.e., local extrema at the same locations). Thus, all the applications demonstrated in [3] (depth-camera odometry and mapping, path planning, surface reconstruction) can be performed with the proposed method. In this paper, we consider novel uses of GP-based distance fields such as echolocation and mapping with UGW sensing systems.

A. Echolocation

The first application is the global localisation of a system consisting of an omnidirectional ultrasonic emitter-receiver in contact with the structure, that can eventually be used for automated long-range inspection of large metal structures [7]. At every measurement step i , a time signal $s(t)$ is pulsed by the emitter to create an UGW that propagates radially around the emitter, *inside* the structure’s material. Simultaneously, the receiver collects the measurement that contains the ultrasonic echoes due to reflections of the excited wave on structural features. Following the terminology of Section III, we will use the term surface \mathcal{S} to denote the set of structural features (i.e. metal panels’ boundaries in the present work, but could include other features such as stiffeners and potential defects) that reflect the UGWs. Further information about the nature of the measurements is provided in Appendix A. The objective is to estimate the system’s position \mathbf{x}_i by relying on ultrasonic measurements, noisy odometry information, and given the map in the form of a point cloud.

For this localisation problem, as mentioned above, let us consider that the surface \mathcal{S} is known in the form of a point

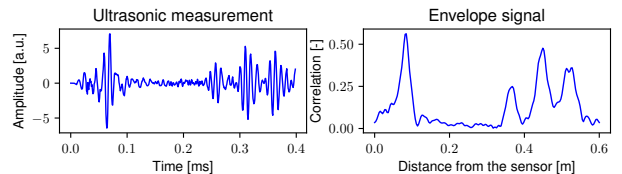


Fig. 5. Example of an acoustic measurement acquired on an aluminium plate (top plot) and the corresponding envelope signal obtained by correlating the measurement with a wave propagation model (bottom).

cloud. To recover the position of a moving emitter-receiver, we rely on a particle filter, as in [7]. Such filters can usually provide satisfactory solutions to the localisation problem when the dynamic and observation models are non-linear, and the process and measurement noises are non-Gaussian [46], as in our case study. Yet, the method described in [7] can only be applied to metal panels with a rectangular shape. Hence, we propose a modification to the calculation of the particles’ weights to make the approach applicable to arbitrary surface geometries, using the proposed GP-based distance field.

The modified localisation approach requires the determination of envelope signals $e_i(d)$, where d is the distance to the emitter-receiver. $e_i(d)$ measures the similarity between the ultrasonic measurement and the signal that would be obtained after reflection at a distance d from the emitter-receiver, based on a wave propagation model (see Appendix A). The envelope signal ranges between 0 and 1, and it presents a local maxima in d if there is indeed a reflector at such distance, as illustrated in Fig. 5. The figure shows a distinguishable first echo that indicates the presence of a plate boundary at 0.08 m, and late echoes that will be considered as noise. The equations used to derive the envelope signals from the ultrasonic measurements are found in Appendix A. As a first step towards localisation with arbitrary surfaces, we only rely on the detection of the echo due to reflection on the closest surface element. We propose the particle filter using the following expression for the particles’ weight:

$$w_i^n = \eta \exp \left\{ \alpha e_i(\hat{d}(\mathbf{x}_i^n)) - \beta \hat{d}^2(\mathbf{x}_i^n) \right\}, \quad (12)$$

where $\hat{d}(\mathbf{x}_i^n)$ is the distance of the n -th particle to the closest point on the surface \mathcal{S} computed with (8), η is the normalization factor, and α and β are positive parameters. The term in $\hat{d}^2(\mathbf{x}_i^n)$ is a prior used to account for the fact that the reception of the first ultrasonic echo is less likely at a larger distance. Note that a simpler measurement model that would not consider such a regularization term can also be used, but it will be less robust to the presence of late echoes.

B. Mapping

For the purpose of mapping, the goal is to estimate the continuous distance field given the system’s localisation and UGW measurements as described in the previous subsection. For the sake of simplicity, we will only consider the first maxima of $e_i(d)$ as a direct measurement d_i of the distance to surface from position \mathbf{x}_i . Accordingly, given the measurement d_i at the known position \mathbf{x}_i and using (8), the mapping

Method	RMSE error [m]	RMSE std. dev. [m]
Ours RQ	0.011473	0.005506
Ours Matern 3/2	0.014782	0.004642
Ours SE	0.025676	0.016684
Ours Matern 1/2	0.025970	0.003868
Ours Matern 1	0.026370	0.003845
LogGPIS [2]	0.062532	0.003546
Smooth min	0.010354	0.005873

TABLE II
AVERAGE RMSE AND STANDARD DEVIATION OVER 100 DIFFERENT
SIMULATED ENVIRONMENTS (100 × 1600 SAMPLES)

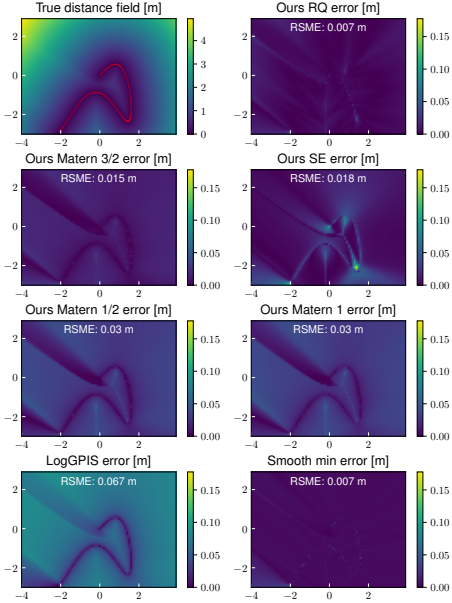


Fig. 6. Accuracy comparison of the proposed distance field with different kernels, LogGPIS [2], and the smooth minimum function. The surface samples are shown in red.

formulation consists in a non-linear least-square optimisation problem with the cost function

$$c(\mathbf{X}) = \sum_{i=1}^Q \|d_i - \hat{d}(\mathbf{x}_i, \mathbf{X})\|_{\sigma_{d_i}}^2. \quad (13)$$

Intuitively, it corresponds to the estimation of pseudo observations \mathbf{X} of the surface \mathcal{S} .

V. EXPERIMENTS

A. Distance field

In this subsection, we benchmark the proposed method against LogGPIS [2] and the simple smooth minimum function applied to the pairwise distances between the query point \mathbf{x} and the surface data $\left(\sum_{i=1}^Q \|\mathbf{x} - \mathbf{x}_i\| \exp(\lambda \|\mathbf{x} - \mathbf{x}_i\|)\right) / \left(\sum_{i=1}^Q \exp(\lambda \|\mathbf{x} - \mathbf{x}_i\|)\right)$. As per its continuous, differentiable nature, the smooth minimum function can be used in place of the LogGPIS in all the applications mentioned in [3]. We use $\lambda = -100$ in the following of this section.

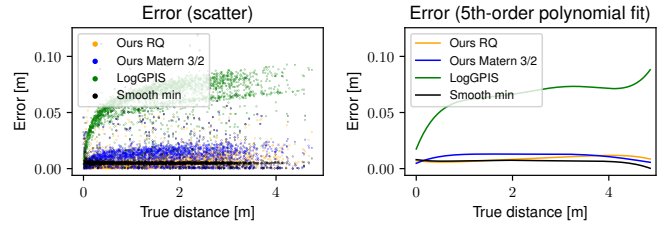


Fig. 7. Comparison of the error distribution of the proposed method with the rational quadratic and $\nu = 3/2$ Matern kernels against LogGPIS [2] and the smooth minimum function (2500 samples randomly queried across 100 different simulated environments).

One hundred simulated 2D environments using the sum of sine functions with both random amplitudes and frequencies have been generated. For each environment, 1600 distance measurements are queried from the field according to a regular grid and the Root Mean Squared Error (RMSE) against the true field is computed. Table II reports the average and standard deviation of the RMSE for each method. One occurrence is illustrated in Fig. 6 with the true distance field and the surface samples (top left) and the absolute error for the inferred field with the different kernels and methods. In Fig. 7 we display the error of 2500 randomly selected inferences across the 100 × 1600 query points aforementioned. Throughout these various visualisations, we demonstrate that the proposed method significantly outperforms LogGPIS. Out of the different kernels and associated reverting functions, the RQ ($\alpha = 100$) and $\nu = 3/2$ Matern kernels provide the best performance and display a level accuracy similar to the smooth minimum function.

It is important to note that the benchmark above uses densely modelled surfaces (red dots in Fig. 6). This is favourable to the smooth minimum function as it does not possess any interpolation abilities. In Fig. 8, we show that in the presence of sparse data, the accuracy of the smooth minimum function is decreased. As mentioned earlier, LogGPIS requires a small lengthscale l to satisfy its base assumption and provide a minimum level of accuracy. However, in the presence of sparse data, a larger l is required to interpolate the surface between measurements. As illustrated in the middle row of Fig. 8, the accuracy of LogGPIS is negatively impacted by an increase of l . The proposed method can accommodate sparse data by increasing the lengthscale l (Fig. 8 bottom row).

B. 3D scan registration

This subsection aims at providing the reader with evidence that the proposed distance field can be used similarly to LogGPIS [3]. While the previous subsection highlights the better performance of the proposed method at predicting the true distance, this characteristic is not needed to perform odometry with point cloud registration, nor for planning. For point cloud registration, the field needs to be minimal on the surface and monotonically increase with the distance to the surface. For planning, the field needs to be maximal the furthest away from the surfaces (eg., the field should be maximal in the middle of a corridor) and monotonically decreasing closer to the surface.

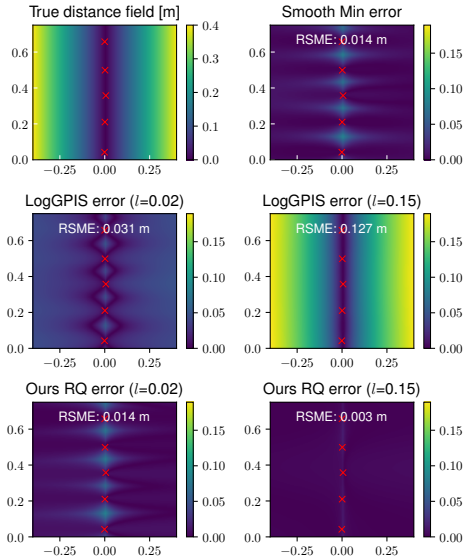


Fig. 8. Illustration of the interpolation abilities of the proposed method against LogGPIS [2] and the smooth minimum function.

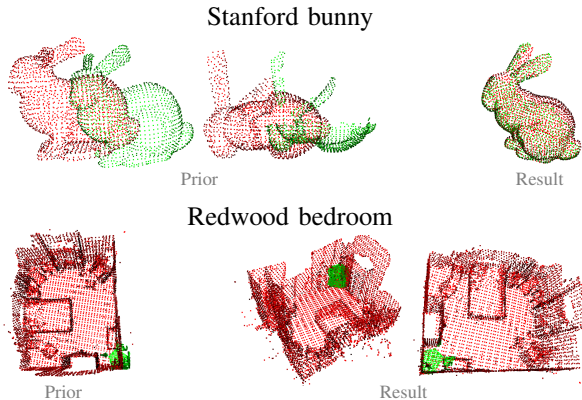


Fig. 9. Point cloud registration using the proposed continuous distance field (map in red and scan in green).

Accordingly, we expect LogGPIS and the proposed method to perform similarly in such applications.

Considering the problem of 3D point cloud registration, we compare LogGPIS and the proposed method (with RQ kernel and $\alpha = 100$) on the Stanford bunny [47] and the Redwood [48] datasets. In both datasets, a map/reconstruction (in red in Fig. 9) is used to generate the continuous distance field $\hat{d}(\mathbf{x})$. A laser scan (in green in Fig. 9) is registered by minimising

$$\operatorname{argmin}_{\mathbf{R}, \mathbf{p}} \sum_{i=0}^Q \left(\hat{d}(\mathbf{R}\mathbf{x}_i + \mathbf{p}) \right)^2, \quad (14)$$

with \mathbf{x}_i ($i = 1 \dots Q$) the 3D points of the scan. The point-to-point RMSE between the scan registered with LogGPIS and the proposed method (RQ kernel) is $8.86\text{e-}5$ m for the Stanford bunny, and $2.46\text{e-}3$ m for the Redwood bedroom.

C. Echolocation

To support robot localisation based on the proposed distance field (with RQ kernel and $\alpha = 100$), we test the proposed

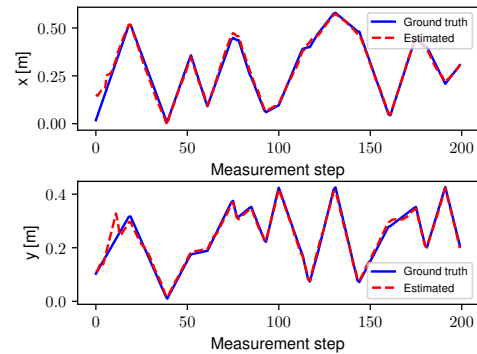


Fig. 10. Localisation results achieved with the particle filter in the simulated scenario.

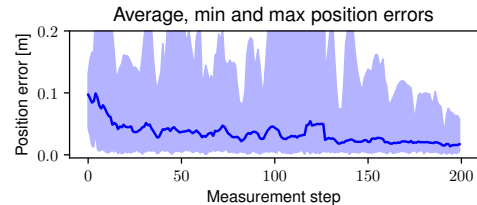


Fig. 11. Localisation results achieved with the particle filter for 20 repetitions of the experiment in simulation. The solid line represents the mean position error, while the upper and lower bounds of the coloured area represent the minimum and maximum errors respectively.

particle filter in simulation and in a real-world setting by using experimental ultrasonic measurements acquired on a metal panel. We consider the same setup for the two scenarios, where the UGW propagates in an aluminium metal panel with dimensions $600 \times 450 \times 6$ mm.

1) *Simulation*: We create robot paths by randomly generating successive linear and rotational displacements, with a maximum of 3cm between two successive measurement points. The excitation $s(t)$ is a two-tone burst sinusoidal wave at 100 kHz. The ultrasonic measurements are simulated using the image source model and an approximate wave propagation model, as presented in Appendix A. We also add Gaussian noise to the simulated data to maintain a fixed signal-to-noise ratio: $\text{SNR} = 10\text{dB}$. The noisy odometry inputs are generated by adding zero-mean Gaussian noise to the ground truth translation ($\sigma_{\text{translation}} = 0.3\text{cm}$) and rotational ($\sigma_{\text{rotation}} = 0.05\text{rad}$) displacements, which are next presented as inputs to the particle filter.

Fig. 10 shows the localisation results, obtained as the median coordinates of the particles, achieved with the filter in the simulated scenario. It can be observed that, despite imperfect initialization of the filter, the position estimate converges to the ground truth position with centimetre accuracy. To assess the repeatability of the result, the experiment is repeated 20 times, where a new trajectory and noisy odometry inputs are generated for each run. Fig. 11 shows the evolution of the average, minimum, and maximum position errors over the 20 runs. It can be seen that, after the convergence of the filter, a centimetre position accuracy is consistently achieved.

2) *Real-world*: We acquire experimental measurements in a laboratory environment with the following procedure: an

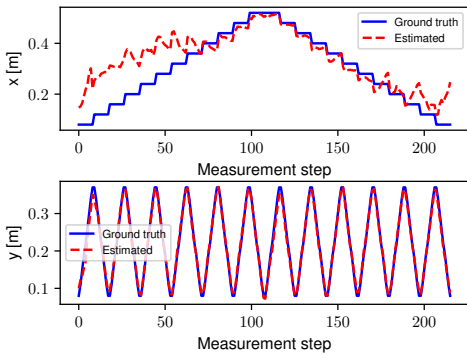


Fig. 12. Localisation results achieved with the particle filter in the real-world scenario.

emitter/receiver pair of nearly collocated transducers, as depicted by Fig. 1, is placed by hand on the vertices of a 9×12 regular grid whose positions are carefully recorded. For every position, the same excitation signal as in the previous scenario is used to generate the UGW, while the receiver collects the ultrasonic response. In total, 108 measurements were acquired. We simulate a “lawn-mower” trajectory as a robot path by using the theoretic displacement between the corresponding measurement positions as ground-truth odometry. In the same way as in the previous scenario, we add zero-mean Gaussian noise to the resulting translation and rotational data to generate the noisy odometry inputs.

Fig. 12 shows the localisation results achieved in this scenario. It can be observed that the coordinate y is estimated within centimetre accuracy, all along the trajectory. However, this is not the case for x , even though the estimate vaguely converges to the true x before slightly diverging again. This can be explained by the fact that we only rely on the echo from the closest surface point for localisation, whereas most of the data has been acquired for sensor positions closer to a vertical boundary than a horizontal one. It is clear that the multiple echoes contained in the measurements should be leveraged in the future to improve the localisation accuracy. Overall, these results support the relevance of using distance fields for localisation, without relying on geometric assumptions on the surface S .

D. Mapping

Similarly to the echolocation case, we first validate our model with a simulated environment before performing mapping in the real world with an emitter-receiver ultrasound sensor. These experiments use the RQ kernel with $\alpha = 100$.

1) *Simulation*: We run a 20-run Monte Carlo simulation using random surfaces, generated as in Section V.A, in a 3×2 m area. Simulated measurements are created by uniformly sampling 300 locations in the 3×2 m area, querying the ground-truth distance field, and adding Gaussian noise with a standard deviation of 0.005 m. The left side of Fig. 13 shows one occurrence of the Monte Carlo analysis with RMSE of 0.031 m. One can see that the error is mostly due to the corridor-like feature in the top right corner of the mapped area

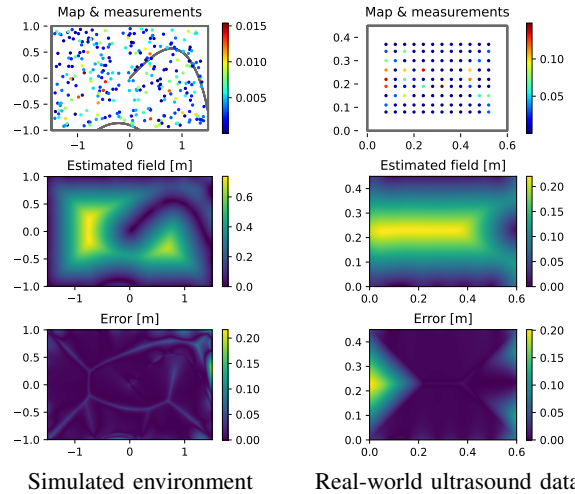


Fig. 13. Continuous distance field mapping with simulated and real-world data. The points in the first row represent the location of the distance measurements. Their colour is the error of the measurements compared with the ground truth of the distance field.

where few measurements are collected (insufficient information). Over the 20 runs, the average RMSE is 0.025 m with a standard deviation of 0.007 m.

2) *Real-world*: The real-world mapping is performed with the same dataset as in the echolocation experiment. The first maxima of the envelope signal are used as direct distance measurements. Fig. 13 (middle right) shows the estimated distance field throughout the aluminium plate. The estimated state field is not perfect and contains large errors on the left side as illustrated in Fig. 13 (bottom right). This can be easily explained by the amount of noise present in the distance measurements. The top right of Fig. 13 displays the error of the measurements. One can see that the areas with high error coincide with highly inaccurate measurements. Overall, the RMSE between the inferred field and the ground truth is 0.045 m and the RMSE of the input measurements is 0.039 m.

While using very limited information (only the first peak of the envelope signal), this experiment shows the potential of the proposed distance field for range-based mapping. We provide in Fig. 15 the probability map obtained with beamforming (Appendix B). The beamforming approach shows more robustness to noisy measurement as it leverages more information from the signals received. However, exploiting such a map for robotic applications is not straightforward.

VI. CONCLUSION

In this paper, we presented a novel GP-based distance field estimation method. Using a point cloud as input, the proposed method first infers an occupancy value based on standard GP regression before applying a kernel reverting function. Through extensive experiments, we show that our method significantly outperforms LogGPIS [2]. This level of accuracy allows for novel applications. This work presents frameworks for echolocation and mapping using UGWs.

Future work will address the variance estimation of the proposed method. In the context of UGW mapping, we will

investigate the use of more information (not only the first peak of the envelope signal) in the GP model to account for the information contained in multiple echoes of the excitation signal. This will result in more robustness with respect to noisy measurements.

VII. ACKNOWLEDGMENT

Cedric Le Gentil and Teresa Vidal-Calleja are supported by the Australian Research Council Discovery Project under Grant DP210101336.

This work has been partially funded by the BugWright2 project, supported by the European Commission under grant agreement 871260 - BugWright2.

REFERENCES

- [1] O. Williams and A. Fitzgibbon, "Gaussian process implicit surfaces," 2007.
- [2] L. Wu, K. M. B. Lee, L. Liu, and T. Vidal-Calleja, "Faithful euclidean distance field from log-gaussian process implicit surfaces," *IEEE Robotics and Automation Letters*, vol. 6, no. 2, pp. 2461–2468, 2021.
- [3] L. Wu, K. M. B. Lee, and T. Vidal-Calleja, "Log-gpismop: A unified representation for mapping, odometry and planning," *arXiv preprint arXiv:2206.09506*, 2022.
- [4] C. E. Rasmussen and C. K. I. Williams, *Gaussian Processes for Machine Learning*. The MIT Press, 2006.
- [5] J.-P. A. Ivan, T. Stoyanov, and J. A. Stork, "Online distance field priors for gaussian process implicit surfaces," *IEEE Robotics and Automation Letters*, vol. 7, no. 4, pp. 8996–9003, 2022.
- [6] H. Lamb, "On waves in an elastic plate," *Proceedings of the Royal Society of London. Series A, Containing papers of a mathematical and physical character*, vol. 93, no. 648, pp. 114–128, 1917.
- [7] O.-L. Ouabi, P. Pomarede, M. Geist, N. F. Declercq, and C. Pradalier, "Monte-carlo localization on metal plates based on ultrasonic guided waves," in *International Symposium on Experimental Robotics*. Springer, 2021, pp. 345–353.
- [8] C. Cadena, L. Carlone, H. Carrillo, Y. Latif, D. Scaramuzza, J. Neira, I. Reid, and J. J. Leonard, "Past, present, and future of simultaneous localization and mapping: Toward the robust-perception age," *IEEE Transactions on Robotics*, vol. 32, no. 6, pp. 1309–1332, 2016.
- [9] R. Mur-Artal and J. D. Tardós, "ORB-SLAM2: an open-source SLAM system for monocular, stereo, and RGB-D cameras," *IEEE Transactions on Robotics (T-RO)*, vol. 33, no. 5, pp. 1255–1262, 2017.
- [10] T. Schneider, M. T. Dymczyk, M. Fehr, K. Egger, S. Lynen, I. Gilitschenski, and R. Siegwart, "maplab: An open framework for research in visual-inertial mapping and localization," *IEEE Robotics and Automation Letters*, 2018.
- [11] T. Qin, P. Li, and S. Shen, "Vins-mono: A robust and versatile monocular visual-inertial state estimator," *IEEE Transactions on Robotics*, 2018.
- [12] A. Elfes, "Using occupancy grids for mobile robot perception and navigation," *Computer*, vol. 22, no. 6, pp. 46–57, 1989.
- [13] A. Hornung, K. M. Wurm, M. Bennewitz, C. Stachniss, and W. Burgard, "Octomap: an efficient probabilistic 3d mapping framework based on octrees," *Autonomous Robots*, pp. 189–206, 2013.
- [14] W. Hess, D. Kohler, H. Rapp, and D. Andor, "Real-time loop closure in 2d lidar slam," in *2016 IEEE International Conference on Robotics and Automation (ICRA)*, 2016, pp. 1271–1278.
- [15] E. G. Tsardoulis, A. Iliakopoulou, A. Kargakos, and L. Petrou, "A review of global path planning methods for occupancy grid maps regardless of obstacle density," *Int. J. of Rob. Res.(IJRR)*, 2016.
- [16] S. T. O'Callaghan and F. T. Ramos, "Gaussian process occupancy maps," *The International Journal of Robotics Research*, vol. 31, no. 1, pp. 42–62, 2012.
- [17] S. Kim and J. Kim, "Building occupancy maps with a mixture of gaussian processes," in *IEEE International Conference on Robotics and Automation (ICRA)*, 2012, pp. 4756–4761.
- [18] S. Izadi, D. Kim, O. Hilliges, D. Molyneaux, R. Newcombe, P. Kohli, J. Shotton, S. Hodges, D. Freeman, A. Davison *et al.*, "Kinectfusion: real-time 3d reconstruction and interaction using a moving depth camera," in *Proc. of the ACM symposium*, 2011, pp. 559–568.
- [19] B. Curless and M. Levoy, "A volumetric method for building complex models from range images," in *Proc. of the Conference on Computer Graphics and Interactive Techniques*, 1996, p. 303–312.
- [20] M. Zucker, N. Ratliff, A. D. Dragan, M. Pivtoraiko, M. Klingensmith, C. M. Dellin, J. A. Bagnell, and S. S. Srinivasa, "Chomp: Covariant hamiltonian optimization for motion planning," *Int. J. of Rob. Res.(IJRR)*, pp. 1164–1193, 2013.
- [21] J. Schulman, Y. Duan, J. Ho, A. Lee, I. Awwal, H. Bradlow, J. Pan, S. Patil, K. Goldberg, and P. Abbeel, "Motion planning with sequential convex optimization and convex collision checking," *The International Journal of Robotics Research*, vol. 33, no. 9, pp. 1251–1270, 2014.
- [22] H. Oleynikova, A. Millane, Z. Taylor, E. Galceran, J. Nieto, and R. Siegwart, "Signed distance fields: A natural representation for both mapping and planning," in *RSS 2016 Workshop: Geometry and Beyond-Representations, Physics, and Scene Understanding for Robotics*, 2016.
- [23] H. Oleynikova, Z. Taylor, M. Fehr, R. Siegwart, and J. Nieto, "Voxblox: Incremental 3d euclidean signed distance fields for on-board mav planning," in *2017 IEEE/RSJ International Conference on Intelligent Robots and Systems (IROS)*, 2017, pp. 1366–1373.
- [24] L. Han, F. Gao, B. Zhou, and S. Shen, "Fiesta: Fast incremental euclidean distance fields for online motion planning of aerial robots," in *2019 IEEE/RSJ International Conference on Intelligent Robots and Systems (IROS)*. IEEE, 2019, pp. 4423–4430.

- [25] J. Ortiz, A. Clegg, J. Dong, E. Sucar, D. Novotny, M. Zollhoefer, and M. Mukadam, “isdf: Real-time neural signed distance fields for robot perception,” *arXiv preprint arXiv:2204.02296*, 2022.
- [26] A. Gropp, L. Yariv, N. Haim, M. Atzmon, and Y. Lipman, “Implicit geometric regularization for learning shapes,” *arXiv preprint arXiv:2002.10099*, 2020.
- [27] J. J. Park, P. Florence, J. Straub, R. Newcombe, and S. Lovegrove, “DeepSDF: Learning continuous signed distance functions for shape representation,” in *Proceedings of the IEEE/CVF conference on computer vision and pattern recognition*, 2019, pp. 165–174.
- [28] B. Mildenhall, P. P. Srinivasan, M. Tancik, J. T. Barron, R. Ramamoorthi, and R. Ng, “NeRF: Representing scenes as neural radiance fields for view synthesis,” *Communications of the ACM*, vol. 65, no. 1, pp. 99–106, 2021.
- [29] L. Mescheder, M. Oechsle, M. Niemeyer, S. Nowozin, and A. Geiger, “Occupancy networks: Learning 3d reconstruction in function space,” in *Proceedings of the IEEE/CVF conference on computer vision and pattern recognition*, 2019, pp. 4460–4470.
- [30] E. Sucar, S. Liu, J. Ortiz, and A. J. Davison, “imap: Implicit mapping and positioning in real-time,” in *Proceedings of the IEEE/CVF International Conference on Computer Vision*, 2021, pp. 6229–6238.
- [31] A. Rosinol, J. J. Leonard, and L. Carlone, “NeRF-slam: Real-time dense monocular slam with neural radiance fields,” *arXiv preprint arXiv:2210.13641*, 2022.
- [32] Z. Zhu, S. Peng, V. Larsson, W. Xu, H. Bao, Z. Cui, M. R. Oswald, and M. Pollefeys, “Nice-slam: Neural implicit scalable encoding for slam,” in *Proceedings of the IEEE/CVF Conference on Computer Vision and Pattern Recognition*, 2022, pp. 12786–12796.
- [33] D. Driess, J.-S. Ha, M. Toussaint, and R. Tedrake, “Learning models as functionals of signed-distance fields for manipulation planning,” in *Conference on Robot Learning*. PMLR, 2022, pp. 245–255.
- [34] M. Adamkiewicz, T. Chen, A. Caccavale, R. Gardner, P. Culbertson, J. Bohg, and M. Schwager, “Vision-only robot navigation in a neural radiance world,” *IEEE Robotics and Automation Letters*, vol. 7, no. 2, pp. 4606–4613, 2022.
- [35] M. Pantic, C. Cadena, R. Siegwart, and L. Ott, “Sampling-free obstacle gradients and reactive planning in neural radiance fields (nerf),” *arXiv preprint arXiv:2205.01389*, 2022.
- [36] B. Lee, C. Zhang, Z. Huang, and D. D. Lee, “Online continuous mapping using gaussian process implicit surfaces,” in *2019 International Conference on Robotics and Automation (ICRA)*, 2019.
- [37] K. Crane, C. Weischedel, and M. Wardetzky, “Geodesics in heat: A new approach to computing distance based on heat flow,” *ACM Transactions on Graphics (TOG)*, vol. 32, no. 5, October 2013.
- [38] S. R. S. Varadhan, “On the behavior of the fundamental solution of the heat equation with variable coefficients,” *Communications on Pure and Applied Mathematics*, vol. 20, pp. 431–455, 1967.
- [39] I. Dokmanić, L. Daudet, and M. Vetterli, “From acoustic room reconstruction to slam,” in *2016 IEEE International Conference on Acoustics, Speech and Signal Processing (ICASSP)*. Ieee, 2016, pp. 6345–6349.
- [40] M. Kreković, I. Dokmanić, and M. Vetterli, “Echoslam: Simultaneous localization and mapping with acoustic echoes,” in *2016 IEEE International Conference on Acoustics, Speech and Signal Processing (ICASSP)*. Ieee, 2016, pp. 11–15.
- [41] D. Ribas, P. Ridao, J. D. Tardós, and J. Neira, “Underwater slam in a marina environment,” in *2007 IEEE/RSJ International Conference on Intelligent Robots and Systems*. IEEE, 2007, pp. 1455–1460.
- [42] M. Y. Cheung, D. Fourie, N. R. Rypkema, P. V. Teixeira, H. Schmidt, and J. Leonard, “Non-gaussian slam utilizing synthetic aperture sonar,” in *2019 International Conference on Robotics and Automation (ICRA)*. IEEE, 2019, pp. 3457–3463.
- [43] R. Worley, Y. Yu, and S. Anderson, “Acoustic echolocation for pipe inspection robots,” in *2020 IEEE International Conference on Multisensor Fusion and Integration for Intelligent Systems (MFI)*. IEEE, 2020, pp. 160–165.
- [44] O. L. Ouabi, P. Pomarede, M. Geist, N. F. Declercq, and C. Pradalier, “A FastSLAM Approach Integrating Beamforming Maps for Ultrasound-Based Robotic Inspection of Metal Structures,” *IEEE Robotics and Automation Letters*, vol. 6, no. 2, pp. 2908–2913, 2021.
- [45] S. Särkkä, “Linear operators and stochastic partial differential equations in Gaussian process regression,” *Artificial Neural Networks and Machine Learning—ICANN 2011*, pp. 151–158, 2011.
- [46] S. Thrun, W. Burgard, D. Fox *et al.*, *Probabilistic robotics*, vol. 1. MIT press Cambridge, 2005.
- [47] G. Turk and M. Levoy, “Zippered polygon meshes from range images,” in *Proceedings of the 21st annual conference on Computer graphics and interactive techniques*, 1994, pp. 311–318.
- [48] J. Park, Q.-Y. Zhou, and V. Koltun, “Colored point cloud registration revisited,” in *ICCV*, 2017.
- [49] Z. Su and L. Ye, *Identification of Damage Using Lamb Waves: From Fundamentals to Applications*, 01 2009, vol. 48.

APPENDIX A

DISTANCE MEASUREMENTS FROM ULTRA-SOUND SIGNALS

The ultrasonic measurements acquired by an emitter-receiver essentially contain the successive echoes due to the reflections of the excited wave on the surface S , i.e., the boundaries of a metal panel in our case study, as illustrated by Fig. 14. These measurements can be modelled by relying on the image source model, which states that the reception of any echo can be interpreted as a signal originating directly from a fictive image source. The image sources positions

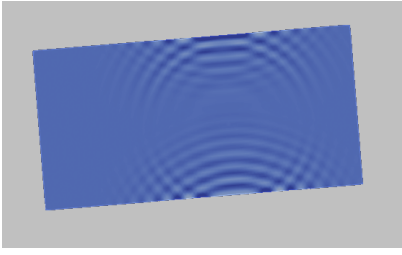


Fig. 14. Guided waves reflected by the edges of a metal plate in a simulation environment.

depend on the position of the actual emitter and the properties of the surface \mathcal{S} . With the assumption that the material is isotropic (i.e., wave propagation is the same in any direction), the propagation transfer is only a function of time and of the distance between the receiver and the image source. This results in the following measurement model:

$$z_i(t) = \sum_{\mathbf{p} \in \mathcal{I}(\mathbf{x}_i, \mathcal{S})} g(\|\mathbf{p} - \mathbf{x}_i\|, t) * s(t) + n_i(t), \quad (15)$$

where $s(t)$ is the excitation used to generate the UGW, \mathbf{x}_i is the emitter position, $\|\cdot\|$ is the Euclidean norm, $\mathcal{I}(\mathbf{x}_i, \mathcal{S})$ is the set of the image sources positions for a surface \mathcal{S} and a real source position \mathbf{x} , $g(\|\mathbf{p} - \mathbf{x}_i\|, t)$ is the acoustic transfer function of the propagation medium, $n(t)$ is an additive Gaussian noise term that we assume temporally and spatially white, and $*$ denotes the convolution operation.

To extract the distance to the closest point of the surface \mathcal{S} from a measurement z_i , we construct correlation signals. They are used to assess the likelihood that a *single* acoustic reflection occurred at any distance d from the emitter-receiver with:

$$z'_i(d) = \frac{\langle z_i(t), \hat{z}(d, t) \rangle}{\sqrt{\langle z_i(t), z_i(t) \rangle \langle \hat{z}(d, t), \hat{z}(d, t) \rangle}}, \quad (16)$$

where $\hat{z}(d, t) = \hat{g}(2d, t) * s(t)$ is the expected signal containing an echo due to a reflection at a distance d , \hat{g} is a propagation model, and $\langle \cdot, \cdot \rangle$ denotes the usual scalar product for time-continuous signals. A standard propagation model for an UGW propagating in a metal panel is

$$\hat{g}(r, \omega) \approx e^{-jk(\omega)r} / \sqrt{k(\omega)r}, \quad (17)$$

where $k(\omega)$ is the wavenumber of the major acoustic mode that usually has a non-linear dependency with respect to the pulsation ω . More details on how to determine this relation given prior information on the plate material can be found in [49]. We subsequently retrieve the envelope of the correlation signals with $e_i(d) = |z'_i(d) + j\mathcal{H}(z'_i)(d)|$, where \mathcal{H} denotes the Hilbert transform operator. Finally, we extract the position of the first local maxima of e_i with a standard peak detector applied to the signal.

APPENDIX B

2D MAPPING WITH DELAY-AND-SUM BEAMFORMING

It is possible to create a 2D (or even 3D) map of acoustic reflectors using a simple Delay-And-Sum (DAS) beamforming

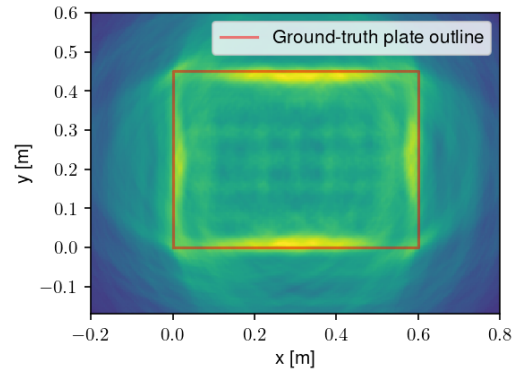


Fig. 15. 2D map obtained by applying DAS beamforming to experimental ultrasonic measurement on a metal panel.

approach. Given a sensor trajectory $\mathbf{x}_{1:T}$ and the corresponding envelope measurements $e_{1:T}$, we build the beamforming map with:

$$\mathcal{L}(\mathbf{x}) = \sum_{i=1}^T e_i(\|\mathbf{x}_i - \mathbf{x}\|), \quad (18)$$

where \mathbf{x} is any point in the map space, to assess the likelihood of presence of a reflector at such position. In Fig. 15, we show the resulting map obtained when DAS beamforming is applied to the dataset of experimental ultrasonic measurements described in the subsection V-C. From the results, we can almost infer the position of the metal panel boundaries that reflected the acoustic wave. However, such map may hardly be used for a task such as echolocation.